SANDIA REPORT

SAND2006-7746
Unlimited Release
Printed December 2006

Simulation of Neutron Displacement Damage in Bipolar Junction Transistors Using High-Energy Heavy Ion Beams

Gyorgy Vizkelethy, Edward S. Bielejec, Barney L. Doyle, Daniel L. Buller,
Robert M. Fleming, Harold P. Hjalmarson

Prepared by
Sandia National Laboratories
Albuquerque, New Mexico 87185 and Livermore, California 94550

Sandia is a multiprogram laboratory operated by Sandia Corporation,
a Lockheed Martin Company, for the United States Department of Energy's
National Nuclear Security Administration under Contract DE-AC04-94AL85000.

Approved for public release; further dissemination unlimited.

Sandia National Laboratories

Issued by Sandia National Laboratories, operated for the United States Department of Energy by Sandia Corporation.

NOTICE: This report was prepared as an account of work sponsored by an agency of the United States Government. Neither the United States Government, nor any agency thereof, nor any of their employees, nor any of their contractors, subcontractors, or their employees, make any warranty, express or implied, or assume any legal liability or responsibility for the accuracy, completeness, or usefulness of any information, apparatus, product, or process disclosed, or represent that its use would not infringe privately owned rights. Reference herein to any specific commercial product, process, or service by trade name, trademark, manufacturer, or otherwise, does not necessarily constitute or imply its endorsement, recommendation, or favoring by the United States Government, any agency thereof, or any of their contractors or subcontractors. The views and opinions expressed herein do not necessarily state or reflect those of the United States Government, any agency thereof, or any of their contractors.

Printed in the United States of America. This report has been reproduced directly from the best available copy.

Available to DOE and DOE contractors from
U.S. Department of Energy
Office of Scientific and Technical Information
P.O. Box 62
Oak Ridge, TN 37831

Telephone: (865) 576-8401
Facsimile: (865) 576-5728
E-Mail: reports@adonis.osti.gov
Online ordering: http://www.osti.gov/bridge

Available to the public from
U.S. Department of Commerce
National Technical Information Service
5285 Port Royal Rd.
Springfield, VA 22161

Telephone: (800) 553-6847
Facsimile: (703) 605-6900
E-Mail: orders@ntis.fedworld.gov
Online order: http://www.ntis.gov/help/ordermethods.asp?loc=7-4-0#online

SAND2006-7746
Unlimited Release
Printed December 2006

Simulation of Neutron Displacement Damage in Bipolar Junction Transistors Using High-Energy Heavy Ion Beams

Gyorgy Vizkelethy, Edward S. Bielejec, Barney L. Doyle, Daniel L. Buller
Department of Radiation Solid Interactions
Robert M. Fleming
Department of Semiconductor Material and Device Science
Harold P. Hjalmarson
Department of Multiscale Computational Material Methods

Sandia National Laboratories
PO Box 5800
Albuquerque, NM 98185-1056

Abstract

Electronic components such as bipolar junction transistors (BJTs) are damaged when they are exposed to radiation and, as a result, their performance can significantly degrade. In certain environments the radiation consists of short, high flux pulses of neutrons. Electronics components have traditionally been tested against short neutron pulses in pulsed nuclear reactors. These reactors are becoming less and less available; many of them were shut down permanently in the past few years. Therefore, new methods using radiation sources other than pulsed nuclear reactors needed to be developed. Neutrons affect semiconductors such as Si by causing atomic displacements of Si atoms. The recoiled Si atom creates a collision cascade which leads to displacements in Si. Since heavy ions create similar cascades in Si we can use them to create similar damage to what neutrons create. This LDRD successfully developed a new technique using easily available particle accelerators to provide an alternative to pulsed nuclear reactors to study the displacement damage and subsequent transient annealing that occurs in various transistor devices and potentially qualify them against radiation effects caused by pulsed neutrons.

Contents

Introduction....................9
Simulations....................9
Principle of using heavy ions for simulating neutron displacement damage....................10
Difference between ion beam and neutron environment....................11
Basis of damage equivalency....................12
Measurement circuit and board....................13
Fluence measurement....................14
  Beam spot size measurement....................14
  Total charge delivered by the beam....................17
Electronic measurements (pre and post shot)....................18
  Gummel Curves....................18
  IV Characteristics....................19
Measurement protocol....................19
A typical dataset....................20
For low emitter-base voltages (V_{BE}) the gain of the transistor becomes less than one and even at higher V_{BE} the gain is significantly less than the initial gain (~200). 21
Damage equivalency between different ions and neutrons....................24
Deviations from the Messenger-Spratt equation....................26
  Light ions (ionization)....................26
  Heavy ions (end of range effect in the collector)....................28
Deep Level Transient Spectroscopy (DLTS) results....................29
simulation results....................33
Summary....................37
References....................38

Figures

Figure 1 Experimental setup using focused ion beams to simulate neutron damage....................11
Figure 2 Damage creation and ionization profile of a 28 MeV Si beam in Microsemi 2n2222 BJT. 12
Figure 3 Test circuit used in the ion beam experiments. Voltages between points marked by red circles are recorded using 16 and 12-bit channels of a DL750 digital oscilloscope. 13
Figure 4 Test board used in the ion beam experiments. 14
Figure 5 Calibration curve for beam spot images. 15
Figure 6 Beam profile at 10 and 100 μs pulse lengths....................16
Figure 7a and b Beam spot overlayed on the image of a device (a), distribution of beam intensity (b)....................16
Figure 8 Typical output of an Ortec 142A charge sensitive preamplifier and its fit to the theoretical response curve. 17
Figure 9 Typical calibration curve for the Ortec 142A preamplifier. 18
Figure 10 Gummel curves before and after the shot. Notice the large increase of the base current that leads to significant gain degradation. 20

Figure 11 Measurement of the total charge delivered before and after the device shot using hundred shots in one second both before and after. The statistical error is around 5%. 21
Figure 12 Base and collector currents during and immediately after a shot. Please not that the current shown here is not the actual base current but only the fraction that goes through the current viewing resistor. Most of the base current is going through the shunt diode to avoid de-biasing the base-collector junction....22
Figure 13 Short term recovery of the transistor gain. 23
Figure 14 Long term recovery of the transistor gain. After a quick recovery up to 1 s the gain is continuously increasing even after 1000 s. 23
Figure 15 Inverse gain degradation as the function of fluence for Si beams with different energies. All the points are on straight lines as predicted by the Messenger-Spratt equation. 24
Figure 16 Inverse gain degradation as the function of 1 MeV neutron equivalent fluence. The neutron data from LANSCE is shown with black squares. The 1 MeV neutron equivalent fluence was calculated using equation **(1.4)**....25
Figure 17 Inverse gain degradation as the function of gamma dose measured at the GIF facilty. The gain degradation saturates around 2 MRad. 27
Figure 18 Inverse gain degradation versus fluence for 12 MeV He ions on virgin and pre-irradiated transistors. Notice that the curve of the virgin transistor becomes parallel with the curve of the pre-irradiated transistor abobe $8x10^{11}$ He/cm^2 fluence....27
Figure 19 Inverse gain degradation for high fluences. The 28 MeV Si curve starts to deviate from the linear dependence around $1x10^{14}$ n/cm^2 equivalent fluence while the 48 MeV Si curve still follows the straight line at $1.2x10^{15}$ n/cm^2 equivalent fluence. 28
Figure 20 Damage profile of 28 MeV and 48 Mev Si in a 2n2222 BJT. Notice the large difference between the twoo profile in the collector. 29
Figure 21 DLTS spectrum for two samples, one irradiated with a fast neutron fluence of ~ 1 x 1014 n/cm2, the second irradiated with heavy ions (28 MeV Si+4) to a final gain of ~20. Both spectra show three main peaks at the following temperatures: 95 K (VO), 140K (VV) and 240K (VP) for a correlator setting of 0.1 ms. We have normalized the spectrum to the VO peak in both cases to aid in comparison. Strikingly, the VO and VV are in excellent agreement while the difference between the VV/VP peak is currently under investigation. 30
Figure 22 DLTS spectrum for two samples, one irradiated with 48 MeV Si to a ion fluence of $3.0x10^{10}$ ions/cm^2, the second irradiated with a 12 MeV He to an ion fluence of $9.4x10^{12}$ ions/cm^2. Both spectra show three main peaks at the following temperatures: 95 K (VO), 140K (VV) and 240K (VP) for a correlator setting of 0.1 ms. The additional peak between the VV and VP peak in the helium irradiation is associated with ionization. This additional peak shows no dependence on the DLTS correlator setting. 31
Figure 23 DLTS spectra 48 MeV Si^{+7} irradiation for three different fluences. For inverse gain degradation less than 0.50 we observe a linear increase in the VP with fluence. For higher fluence values the DLTS amplitude changes dramatically. 31
Figure 24: The total charge as a function of total dose for an oxide layer. 33

Figure 25: Interface trap density as a function of dose rate. 34
Figure 26: Shows the effect of trapped charge on carrier recombination at bulk traps 35
Figure 27 : Shows a comparison of the simulations with transient annealing data for solar cells taken at two different injection rates. 35
Figure 28 : Simulations of DLTS spectra for divacancy defects in a diode. 36

This page intentionally left blank

INTRODUCTION

The electronics of our weapons will be subjected to radiation from hostile countermeasures and possibly from fratricide from friendly weapons exploding in the vicinity. A significant part of this radiation includes short, high fluence neutron pulses. To make sure that the electronics in our weapons work when required it has to be tested against these threats. In the past these tests were carried out at pulsed nuclear reactors, such as the ones at Aberdeen, White Sands Missile Range (WSMPR), and at the Sandia Pulsed Reactor (SPR). The Aberdeen site was shut down more than a year ago, SPR was taken out of commission on October 1, 2006, and WSMR's future is uncertain. There is a therefore a time-critical need to find alternative methods to test the electronic components of our weapons. One of the important components are silicon bipolar junction transistors (BJTs) and our study focuses on them.

Neutrons cause displacement damage in the base region of the BJTs leading to the degradation of their amplification gain. To further complicate matters, the defects anneal with a complex temporal behavior, which depends on the atomic nature of the defect and the local electron density. This "Transient Annealing" leads to a time-dependant behavior of the amplifier gain, which also must be considered when analyzing and certifying device performance.

Our approach to simulate the effects of neutrons is directly implanting high-energy Si (or other) atoms into the active regions of devices to simulate displacement damage effect. Neutrons affect semiconductors such as Si by causing atomic displacements of Si atoms. The first displacement is caused by the nuclear scattering of the neutron itself, producing a recoil Si atom, which continues through the lattice causing many more displacements via a collision cascade. The hypothesis this LDRD tests is quite simple: because it is the collision cascade caused by neutron-recoiled energetic Si atoms that causes most of the damage to the Si semiconductor crystal, why not just implant Si (or other heavy) ions themselves to simulate the production of this damage?

Of course this is somewhat oversimplified, and although, the heavy ion irradiation seems to be similar to neutron irradiation there are significant differences between them, as we will discuss them in the next sections. The main goal of this LDRD was to develop reliable beam diagnostics, establish damage equivalence between various ion beams and reactor neutrons, and determine the effect of photocurrent created by the ion beam on both the experimental setup and on the physics of transient annealing.

SIMULATIONS

The main purpose of the simulations was to develop insight about the oxide effects. In general, these effects are complicated and they are focus of research. To make progress, simulations of some key effects were included to illustrate the mechanisms that must be included in more complete and realistic simulation.

The simulations included the transport of electrons and holes in both the silicon and the silicon dioxide layers. Also included were defect reactions in both the silicon and the oxide. For the silicon, these reactions begin with the creation of interstitials and vacancies by the neutron irradiation or the ion irradiation. These defects recombine electrons and holes, leading to the increased based current observed for bipolar transistors. The photocurrent leads to a transient current during the irradiation. In addition, it can accelerate certain defect reactions involving interstitials.

The oxide reactions are stimulated by the generation of electrons and holes. The holes produce the primary effects. They produce interface traps and also trapped charge. Both of these types of defects tend to reduce the gain in npn transistors such as the 2N2222 transistors. The interface traps cause carrier recombination similar to the effects of bulk defects generated by the neutrons or ions. The trapped charge, for p-doped regions, increases the recombination rate of both the interface traps and the bulk traps.

The trapped charge is produced by pre-existing defects. Some of these traps subsequently release hydrogen that migrates to the interface. There the hydrogen reacts with passivated interface traps to produce active interface traps.

The calculations described in this report focused on the following phenomena:

1. The trapped charge in the oxide.
2. The effects of trapped charge on carrier recombination.
3. The effects of photocurrent and injected charge on defect annealing involving interstitials.
4. Direct simulation of DLTS spectra for arbitrary distributions of defects generated by end of range effects.

PRINCIPLE OF USING HEAVY IONS FOR SIMULATING NEUTRON DISPLACEMENT DAMAGE

Pulsed nuclear reactors provide short, high intensity neutron pulses, which in many cases are accompanied with gamma ray irradiation that might last longer than the actual neutron pulse. While the neutrons cause mainly displacement damage these gamma ray pulses cause ionization, which results in photocurrent. The ion beams create both displacement damage and ionization at the same time. We are using a high-energy heavy ion beam from a tandem accelerator focused into a small spot to achieve displacement damage comparable to the damage due to neutrons from pulsed nuclear reactors. In case of the pulsed nuclear reactors the reactor becomes critical, starts producing neutrons then due to its geometry its shuts down in a certain time. Therefore, the neutron flux, pulse length are determined by the design of the reactor and it is quite limited*. Also, the parts and the fixtures used in the tests become activated which makes their handling problematic.

---

* Obviously, the fluence can be controlled by placing the tested part at different distances from the reactor core.

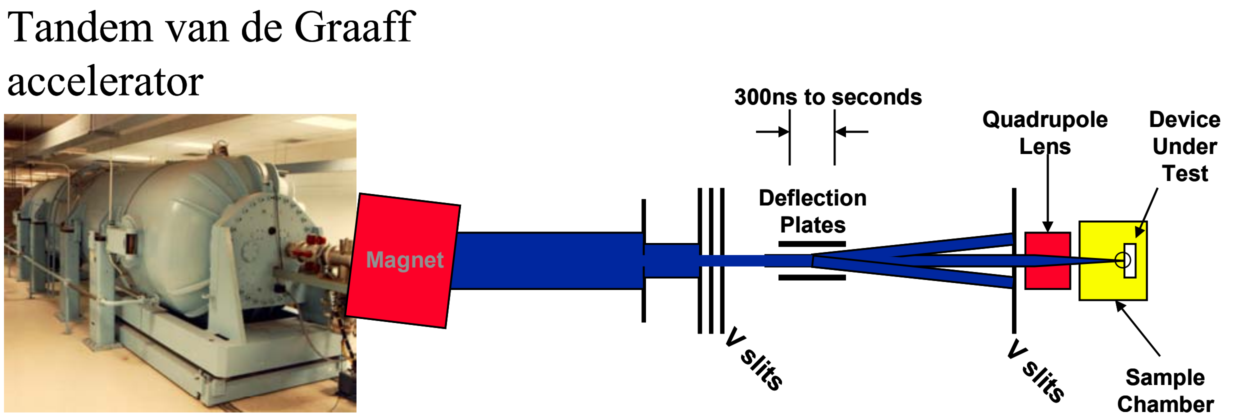

Figure 1 Experimental setup using focused ion beams to simulate neutron damage

In case of the ion beam tests we have a continuous ion beam that we can put on the test devices for an arbitrary time. This way we have precise control of the pulse length, flux (by controlling the ion beam current), and fluence. A typical experimental setup is shown in Figure 1. The heavy ion beam is produced by a tandem Van de Graaff accelerator. The current ranges between a few and a few hundred nAs depending on the energy of the beam and the ion species. Then the ion beam is focused to approximately the same area as the size of the device under test (DUT). Using deflection plates the beam is completely deflected from the devices. A high voltage switch then puts the beam on the DUT for the required time. The pulse width is only limited by the rise and fall times of the HV pulser, which in our case were 150 ns.

DIFFERENCE BETWEEN ION BEAM AND NEUTRON ENVIRONMENT

Although, we intend to use heavy ion beams to simulate neutron damage we need to discuss the differences between the neutron and heavy ion beam environment.

- While neutrons create vacancies uniformly throughout the device, ions loose energy as they travel deeper into the device; therefore, their damage creation and ionization rates change with depth. Figure 2 shows a typical ionization and vacancy creation profile for a 28 MeV Si beam into a Microsemi 2n2222 BJT. The base-emitter junction is at the depth of 4.2 μm and the collector-base junction is at the depth of 6.1 μm in this particular device. From the figure it is clear that the damage in the collector is several times larger than in the base-emitter junction, which can lead to serious problem. Increasing the beam energy or using lighter ions can produce a more uniform damage profile but it significantly reduces the damage creation rate.
- In the neutron experiments it is usually enough to characterize the environment in space and time only once, the neutron flux is quite reproducible. In case of the ion beams the beam parameters (beam current, beam spot shape and intensity distribution, etc.) are usually different from day to day.
- The beam spot of the ion beam is very small in order to achieve high fluxes; it is usually just about the size of the device. This prohibits any kind of real time dosimetry.
- The devices are in vacuum in the ion beam experiments and this can change the characteristics of the operation of the device.

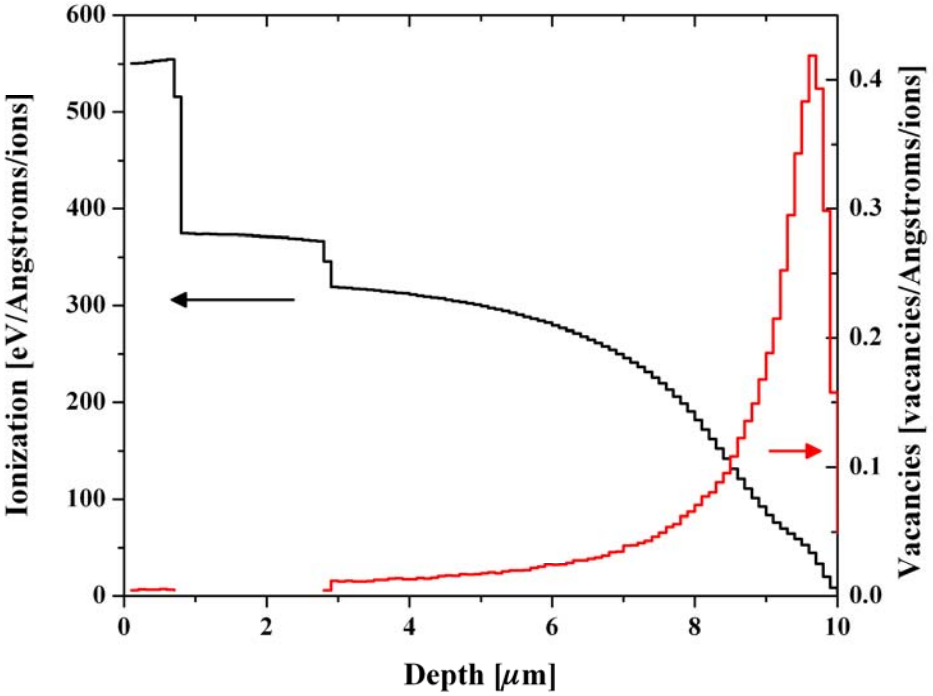

Figure 2 Damage creation and ionization profile of a 28 MeV Si beam in Microsemi 2n2222 BJT.

BASIS OF DAMAGE EQUIVALENCY

Damage equivalence between different kinds of particles has been studied for some time. A recent excellent review is given in[1]. Using various light ions and neutrons on silicon BJTs, Summers *et al*[2] showed that the damage ratio calculated from the Messenger-Spratt equation[3] scales with the Non-Ionizing Energy Loss (NIEL). The Messenger-Spratt equation holds for displacement damage and linearly relates the inverse gain degradation (D), defined by equation (1.1), to the incident fluence.

$$D = \frac{1}{G} - \frac{1}{G_0} \qquad (0.1)$$

where G_0 and G are the initial gain and the final gain respectively. The Messenger-Spratt equation (1.2) defines a damage factor, k, which characterizes the damage to the transistor with Φ being the particle fluence. We will use this k damage factor in the future to compare damage due to different particle types.

$$D = k \cdot \Phi \qquad (0.2)$$

Most of the damage equivalency studies were done with light ions (protons to alphas) and there is very little data available for heavy ions. Warner *et al*[4] reported results for damage equivalency between 2 MeV protons and 22 MeV Si ions in p^+n GaAs solar cells. They concluded that the normalized photocurrent scaled with the displacement damage calculated from the NIEL for both ions. If the same damage equivalency can be established between heavy ions and neutrons, the neutron damage experiments can be simulated in a much simpler and safer environment. Since the inverse gain degradation is proportional to the number of defects (see references 1-3) we decided to use the actual number of vacancies created instead of the NIEL. The vacancy creation rate can be calculated using Monte-Carlo binary collision codes, such as SRIM[5]. As will be shown in the following sections we used SRIM to calculate the vacancy creation rates for various ions and compared them to the 1 MeV equivalent damage kerma defined by ASTM[6].

MEASUREMENT CIRCUIT AND BOARD

The measurement circuit is very similar to the one used in the standard WSMR and SPR experiments as shown in Figure 3. This circuit has been the result of a long process where we determined that standard current and voltage power supplies (such as the Keithley 24xx series) are not able to follow the fast current and voltage changes in the circuit and they provide false results. The results of this circuit development were used in the 2006 SPR-III campaign to test BJTs. This circuit differs from the standard WSMR and SPR circuits in the placement of a shunt diode in the base leg. The reason for this diode is to limit the potential change of the base; therefore, avoid de-biasing the base-collector junction. The diode voltage is set such way that most of the photocurrent goes through the diode. This allows us using a relatively large base current monitoring resistor to measure the base current accurately and keeps the base potential low.

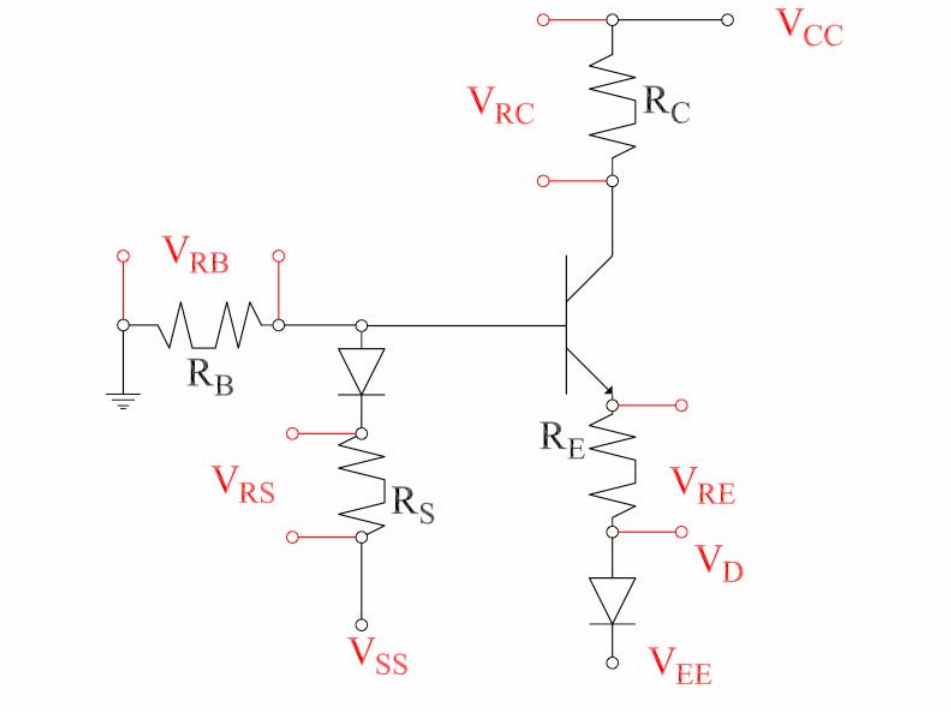

Figure 3 Test circuit used in the ion beam experiments. Voltages between points marked by red circles are recorded using 16 and 12-bit channels of a DL750 digital oscilloscope.

Except for VCC, VEE, VSS, and the temperature all the parameters are recorded on both the 16 and 12-bit channels of a DL750 Yokogawa digital oscilloscope. VCC, VEE, and VSS are recorded only using the 12-bit channels since we expect minimal changes of these parameters. We can test four transistors without braking vacuum using our special board shown in Figure 4.The transistors are embedded in an Al block that used as a heat sink and a Pt thermometer is put into the Al block. The transistor electrodes and the Pt thermometer are connected to SMA and BNC connectors on the outside of the chamber using RG-174 50 Ω cables. Then they are connected with RG-58 50 Ω cables to a standard test board used in the WSMR and SPR experiments. RG-58 cables are used for the connection from the board to the DL750 and to Tektronix PS280 power supply.

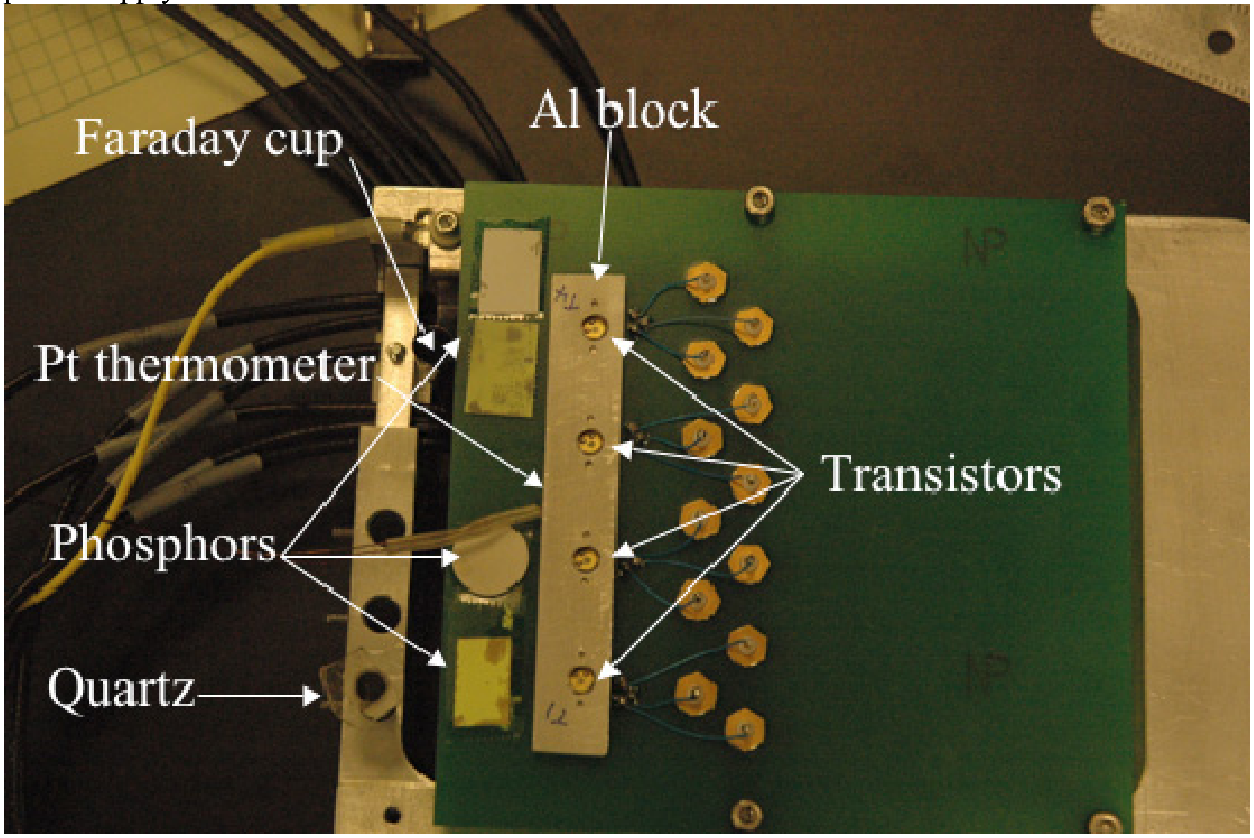

Figure 4 Test board used in the ion beam experiments.

FLUENCE MEASUREMENT

The measured fluence in these experiments is one of the most important parameter. Basically it is determined by two quantities, the area of the ion beam and the total number of delivered particles or the total charge[†]. In the next two sections we describe how we determined the beam spot area and the total number of particles delivered.

Beam spot size measurement

To measure the beam spot size we used ion luminescence. We used a P47 phosphor with a short ion beam pulse and the image was recorded with a CCD camera through the OM-40 microscope. We could not use the real pulse length in many cases since the CCD camera saturated for those pulses. Here we assumed that the light intensity is proportional to the beam current and the exposure time, and the beam shape and intensity distribution does not change with the pulse length. To calibrate the image scale we used an object with sharp contrast. We moved the object to several positions with 50 nm precision and recorded the images. Then the movement of a sharp feature in pixels was compared to the preset movement.

[†] The number of particles can be calculated from the total charge delivered using the charge state of the ions.

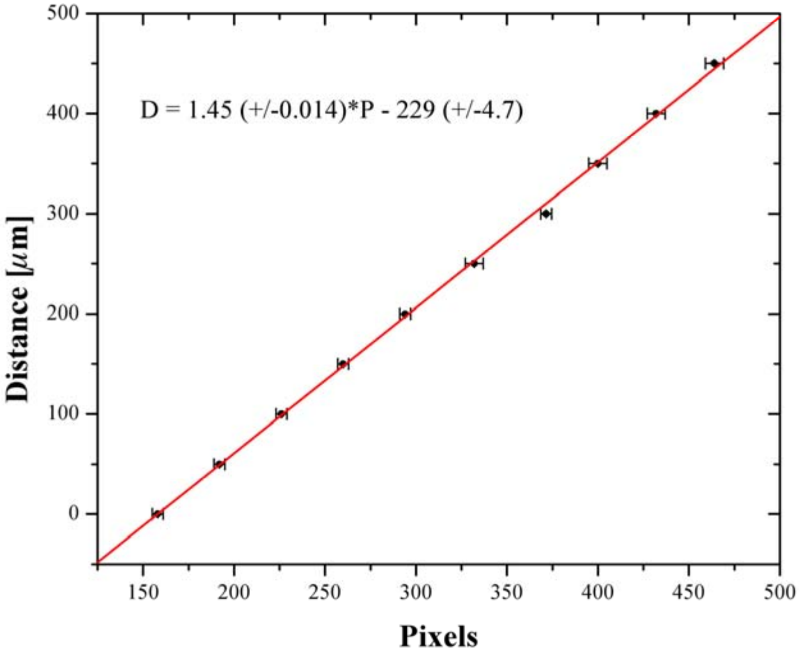

Figure 5 Calibration curve for beam spot images.

Figure 5 shows the result of the calibration. The uncertainty in the pixel measurement is due to the finite sharpness of the object in the images. The images of the ion beam shots were taken at the maximum pulse length where the CCD camera did not saturate. At least ten images were taken in a short time and the area and its statistical uncertainty was calculated. Since the ion beam spot does not have a sharp edge and the P47 did not luminescence for low intensities and short pulses we needed to estimate the halo of the spot. Figure 6 shows cut along the x axis through the center of the image of 10 µs and 100 µs shots at the same current. The curve of the 100 µs shot is divided by 10 to put on the same scale as the 10 µs shot. The 100 µs shot saturated the CCD camera but showed the edges very well. Using these edges and the 10 µs shot we calculated that the beam intensity decays exponentially at the edges with a ~22 µm decay length. Using this decay length we estimate that about 2% of the beam spot is not visible to the CCD camera when we use a pulse length which is just under the saturation limit. From the ten images recorded we usually get about 4-5% uncertainty for the beam spot area.

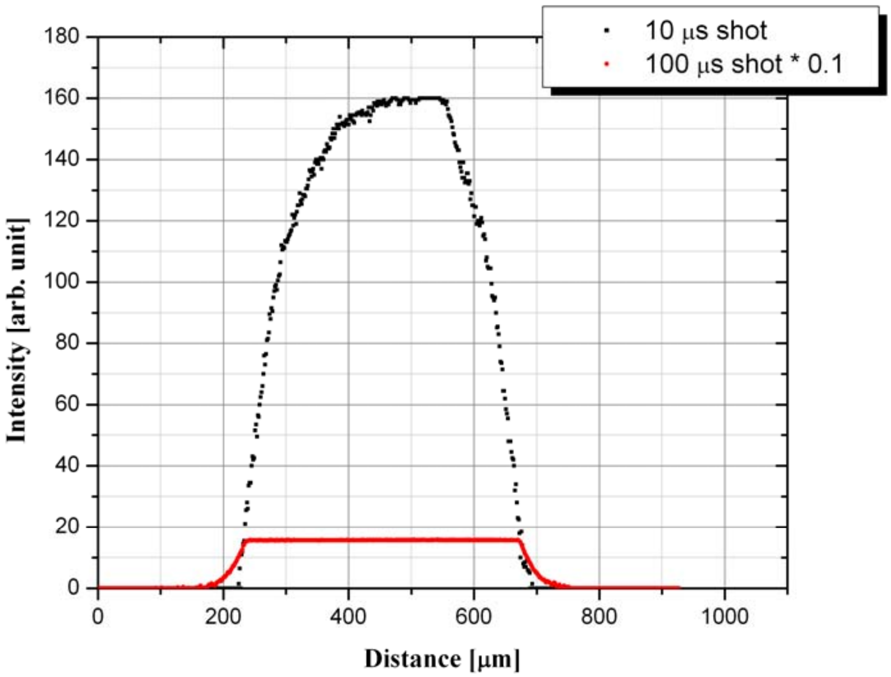

Figure 6 Beam profile at 10 and 100 µs pulse lengths.

Although the beam spot area can be determined with relatively good precision that is not really the flux or fluence uncertainty. Unfortunately, the beam spots of size around 0.5x0.5 mm^2 are not very uniform. Figure 7a shows an overlaid beam spot image over the device. Please note that the structure in the red part of the beam is due to the structure on the device. Figure 7b shows the distribution of the beam intensity. If we calculate the standard deviation over the beam spot we get ~ 55%. On the other hand the standard deviation of the beam intensity over the device is only 18%.

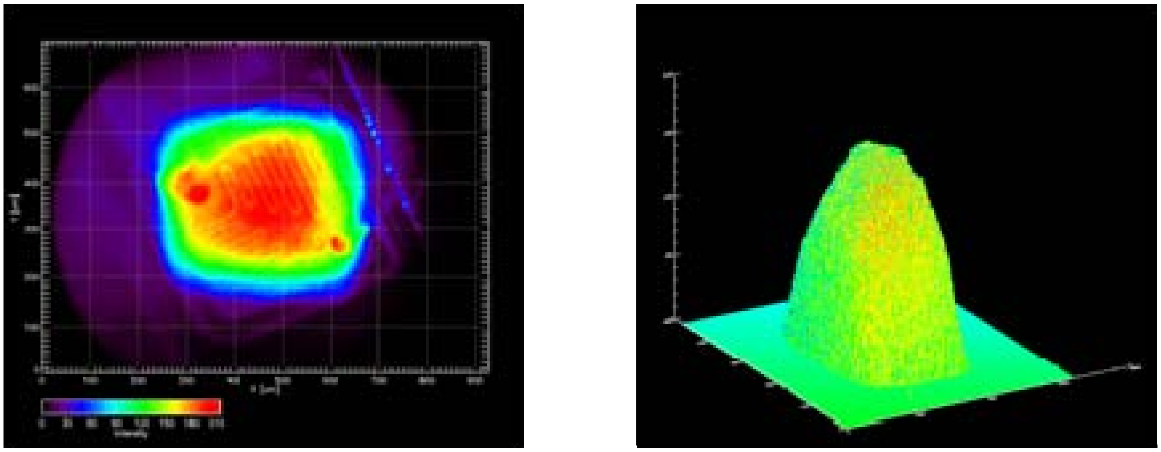

Figure 7a and b Beam spot overlayed on the image of a device (a), distribution of beam intensity (b)

Total charge delivered by the beam

We have to emphasize again that due to the nature of the ion beam setup we cannot measure the total number of ions on the sample. In order to estimate it we measure the total charge of a shot before and after the real shot several times to estimate the total charge delivered in one shot. We measure the current into a Faraday cup in the beam line either using an Ortec 142A charge sensitive preamplifier (low currents and short pulses) or a Keithley 428 current amplifier (longer pulses, higher currents). The charge or the current waveforms are recorded with a Tektronix digital oscilloscope. The waveforms then fitted to the theoretical response curve and the total delivered charge is determined. A typical Ortec 142 waveform and its fit shows in Figure 8. The waveform was fitted using equation (1.3)

$$V(t) = i \cdot (t - t_0) \cdot e^{-\frac{t-t_0}{\tau}} \tag{0.3}$$

The uncertainties of the relevant parameters (pulse length and total charge) from the fit are generally less than 1%.

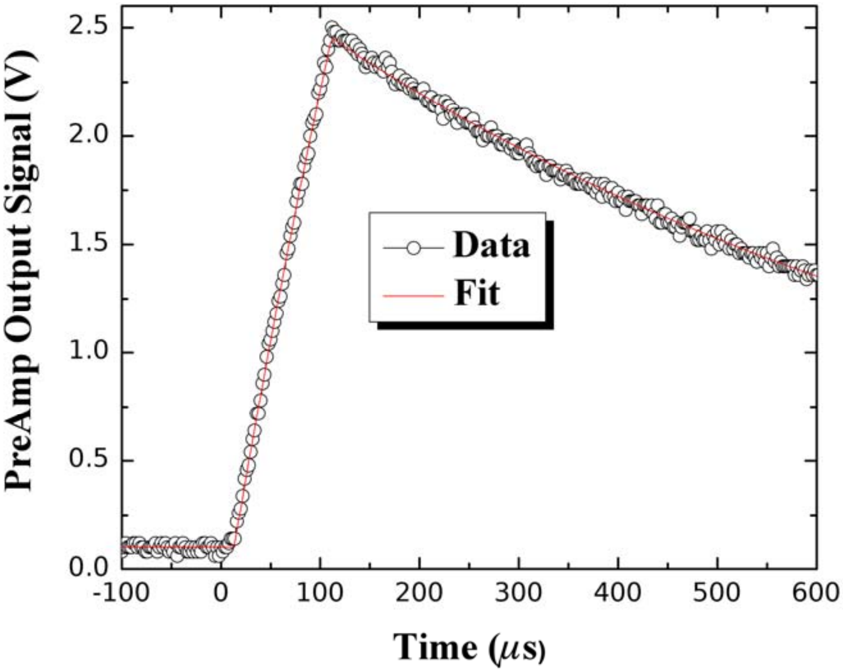

Figure 8 Typical output of an Ortec 142A charge sensitive preamplifier and its fit to the theoretical response curve.

These measurements are performed with the Faraday cup biased at 300 V. Experimental tests showed that the Faraday cup biased at 300 V measures all the current. The Ortec 142 or the Keithley 428 is cross calibrated to a Keithley 6512 electrometer every day or when a new beam is used. Several shots are measured by the Keithley 6512 in charge measurement mode then several shots are measured with either the Ortec 142 or the Keithley 428. In case of the Keithley

6512 the shots are fired as fast the 6512 could measure the charge while in case of the 142 or 428 usually 100 shots are fired in one second. Figure 9 shows a typical calibration curve for the Ortec 142 preamplifier. In a test 100 shots are fired before and after shooting the device in one second. The waveforms are fitted and then the pulse length and total charge are calculated by a weighted (with the uncertainties from the fits) of the parameters.

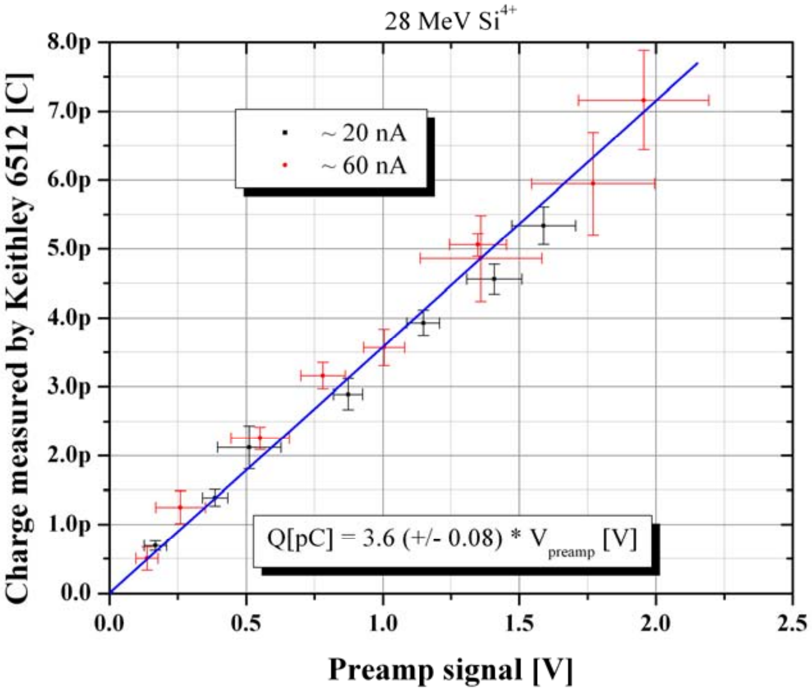

Figure 9 Typical calibration curve for the Ortec 142A preamplifier.

ELECTRONIC MEASUREMENTS (PRE AND POST SHOT)

The following electronics measurements, which include a full suite of Gummel-Poon curves as well as an IV characteristic, were measured with the devices mounted in the vacuum chamber.

Gummel Curves

The Gummel curves were measured using a JD Instruments Parametric Workstation (PWS). Six Gummel curves were measured for each device using the following settings.

- GA1 has the collector at a constant voltage of 5 V, the base at a constant voltage of 0, and the emitter sweeps from 2 to -0.75 V with a step size of -0.005 V.
- GA2 has the collector at a constant voltage of 5 V, the base at a constant voltage of 0, and the emitter sweeps from 2 to -0.3 V with a step size of -0.02 V.
- GB1 has the collector sweep from 2 to -0.75 V with a step size of -0.02 V, the base at a constant voltage of 0, and the emitter at a constant voltage of zero.

- GB2 has the collector sweep from 2 to -0.3 V with a step size of -0.02 V, the base at a constant voltage of 0, and the emitter at a constant voltage of zero.
- GC has the collector at a constant voltage of 0, the base at a constant voltage of 0, and the emitter sweeps from 2 to -0.75 volts with a step size of -0.01 V.
- GD has the collector at a constant voltage of 10 V, the emitter at a constant voltage of 0 V, and the base sweeps from 100 pA to 1.5 mA with a log scale. The collector and emitter currents are set to a limit of 1.2 mA. The GPD measurement technique is also documented in ASTM E1855-05[7].

IV Characteristics

The IV characteristics were measured using a JD Instruments Parametric Workstation (PWS). Two IV curves were measured for each device using the following settings.

- IV_low has the emitter at a constant voltage of 0, the collector sweeps from 0 to 2 volts with a step size of 0.1 V and the base sweeps, at each collector voltage, from 0 to 2 µA, in 9 steps.
- IV_high has the emitter at a constant voltage of 0, the collector sweeps from 0 to 2 volts with a step size of 0.1 V and the base sweeps, at each collector voltage, from 0 to 20 µA, in 9 steps.

MEASUREMENT PROTOCOL

Since the neutron environment is quite different from the ion environment we had to define a different protocol.

1. The lid of the devices are removed (ions are not able to penetrate the device lid) and placed in the vacuum chamber.
2. Pre shot electrical characterization is performed as described above.
3. The sample chamber is pumped down to < 3×10^{-6} mbar. The devices are not powered during the pump down.
4. The ion beam is focused to a somewhat larger spot than the device and the desired current is set.
5. Several sets of shots are taken on a piece of P47 phosphor foil with different pulse length. The image due to the ion luminescence is captured and recorded. These images are used to determine the beam spot size and its uncertainty.
6. The BJT is turned on and all of its parameters monitored until they stabilize.
7. Several shots are fired into a Faraday cup in the beam line in a short time to characterize the shot (usually about 100 shots in 1 second). The Faraday cup is connected to either a charge sensitive amplifier or a current amplifier and the transient is recorded with a digital storage oscilloscope.
8. The Yokogawa DL750 is armed (set to 1 s full scale, 1 MHz sampling rate, and 10M buffer length), the Faraday cup is removed, and one shot is fired at the device.
9. The Faraday cup is reinserted and another set of shots fired and recorded as before.

10. The slow, longer measurement is done either using a second DL750 or by reading the fast DL750 in every second after saving the fast data. This second method produces a 25 second gap between the fast and slow data due to the time it takes to save the fast data.
11. After the slow measurement is done the power to the transistor is turned off.
12. The chamber is vented with the transistor powered down.
13. A second set of electrical measurements is performed, post shot characterization (same set of measurements pre shot).
14. Data is processed, and converted into HDF format.

A TYPICAL DATASET

The data and the figures in this section are from a 28 MeV Si^{4+} shot on a Microsemi 2n2222 npn BJT. The pulse length of the shot was nominally 100 µs with 100 nA ion beam current. The transistor was operated in constant emitter current mode at 0.22 mA emitter current. Figure 10 shows the Gummel curves before and after the shot. There is a significant increase in the base current due to increased recombination because of the displacement damage.

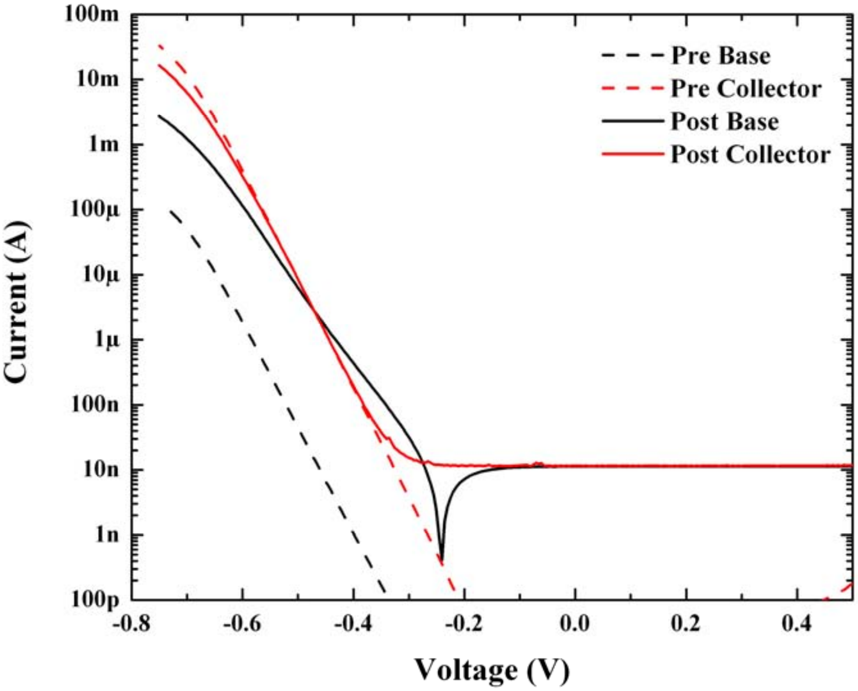

Figure 10 Gummel curves before and after the shot. Notice the large increase of the base current that leads to significant gain degradation.

For low emitter-base voltages (V_{BE}) the gain of the transistor becomes less than one and even at higher V_{BE} the gain is significantly less than the initial gain (~200).

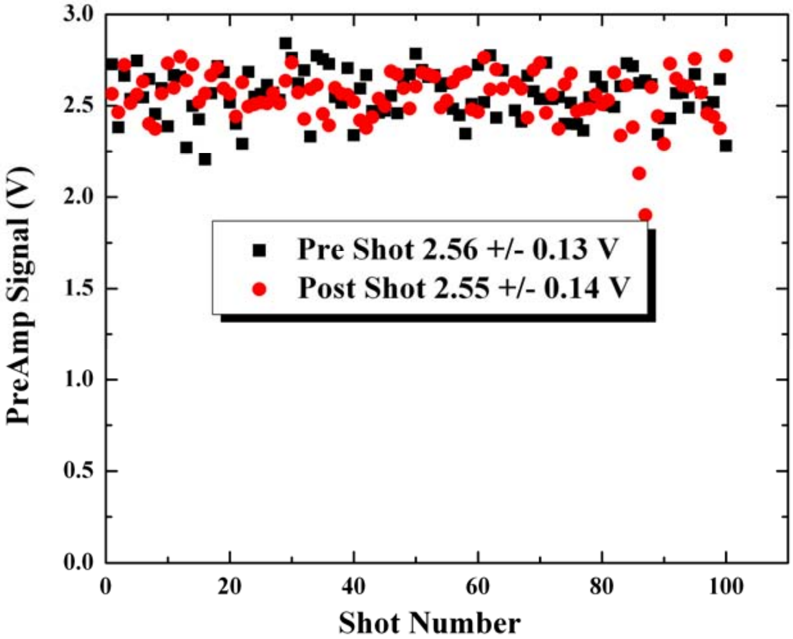

Figure 11 Measurement of the total charge delivered before and after the device shot using hundred shots in one second both before and after. The statistical error is around 5%.

Figure 11 shows the measured total charge delivered with a shot before and after the actual device shot. The measured preamplifier amplitudes (from which the fluence can be calculated) before and after the device shot agree within the statistical error, which is ~5%. This statistical uncertainty was approximately the same for all ion types and energy used.

Figure 12 shows the base and collector currents before, during, and after the shot. There are several features that are worth to discuss.

- During the shot both currents increase, the base current changes sign. It is normally negative but during the shot it becomes positive. When ions go through the transistor they create electron-hole pairs as they loose their energy. In normal operation the base-collector junction of the BJT is reverse biased. The electron-hole pairs are quickly separated in this junction and swept out creating a photocurrent. This photocurrent is measured during the pulse in the base and collector legs.
- Both the base and collector currents decrease during the pulse. This is due to the increasing displacement damage during the pulse. The displacement damage reduces carrier lifetime; therefore, the photocurrent decreases.
- The photocurrent in the device has the same magnitude in both the base and collector electrode because of charge conservation. In this figure the current through the base current viewing resistor is multiplied by 50 to put the currents on the same scale. This illustrates how well the shunt diode (shown in Figure 3) is working. As we discussed above, the role of this diode is to limit the current going through the base current viewing resistor. The total photocurrent through this resistor (~1 kΩ) would be enough to collapse the reverse biased base-collector junction.

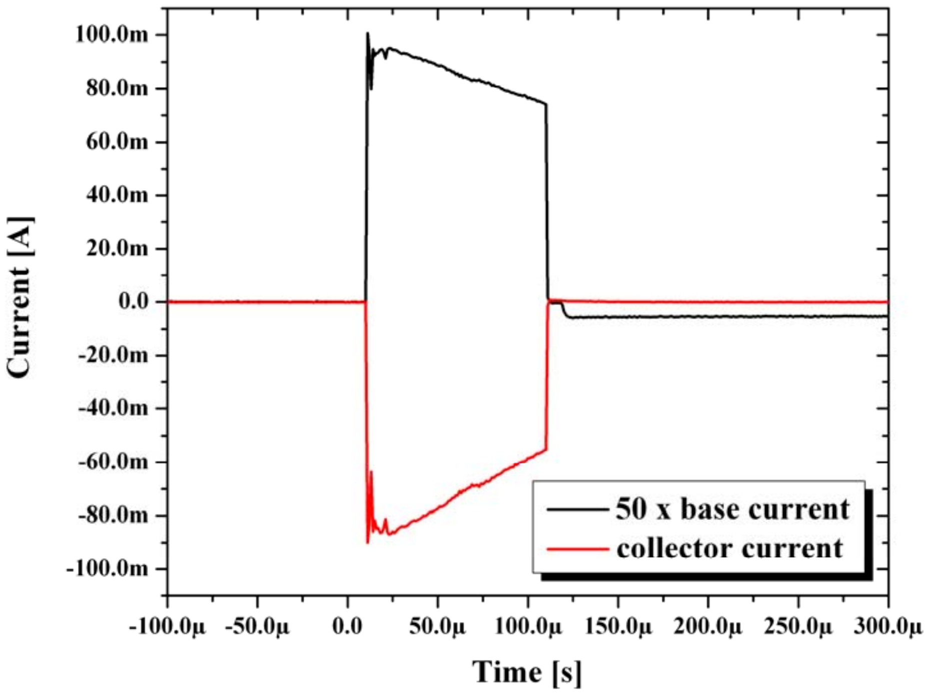

Figure 12 Base and collector currents during and immediately after a shot. Please not that the current shown here is not the actual base current but only the fraction that goes through the current viewing resistor. Most of the base current is going through the shunt diode to avoid de-biasing the base-collector junction.

- After the shot the base current becomes negative again but it is much larger than before. Due to the displacement damage the recombination at the emitter-base interface increased which leads to larger base current and consequently lower gain. In this particular case the gain became less than 1 immediately after the shot. As the damage anneals out the base current decreases and the gain recovers somewhat. Figure 13 and Figure 14 show the short term and long term gain recovery. At short term (up to 1 s) the gain quickly recovers from below one to almost 2. At long term the gain continues recovering up to 2.7 at 1000 s but the gain still increasing, which means that the annealing still continues.

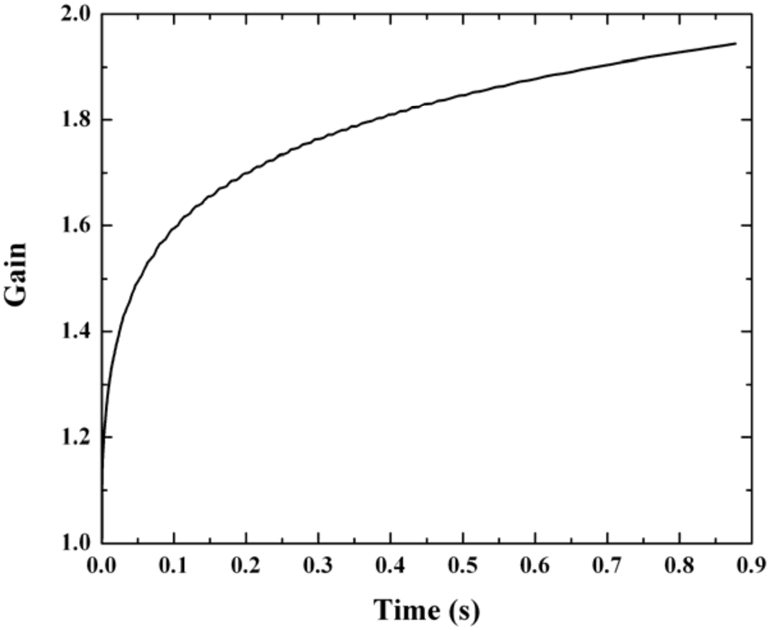

Figure 13 Short term recovery of the transistor gain.

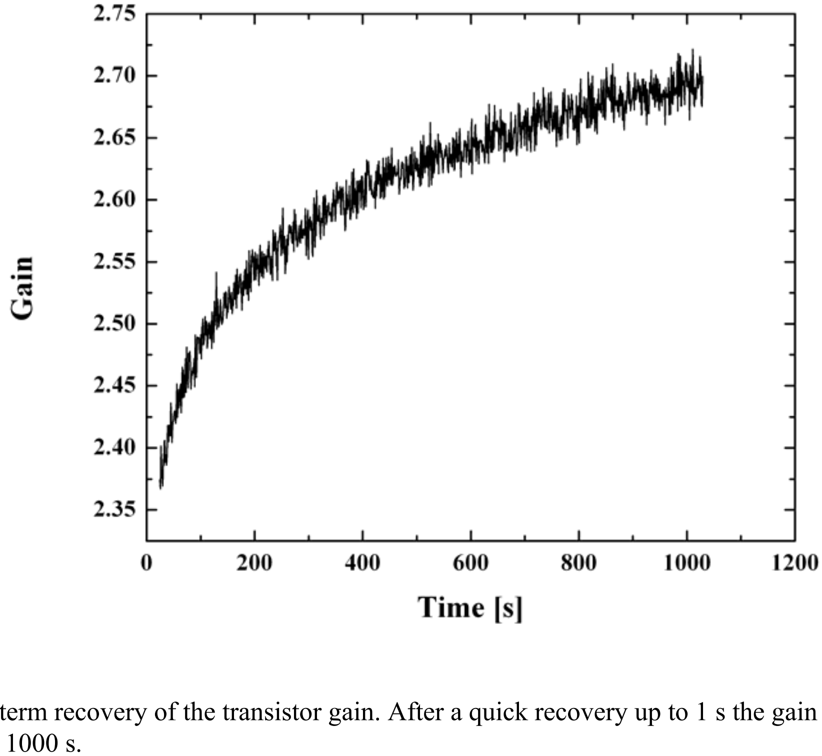

Figure 14 Long term recovery of the transistor gain. After a quick recovery up to 1 s the gain is continuously increasing even after 1000 s.

DAMAGE EQUIVALENCY BETWEEN DIFFERENT IONS AND NEUTRONS

In order to be able to use ion beams to simulate neutron displacement damage a damage equivalency has to be established between ions and neutrons. This damage equivalency is different for different ion species and even for the same species with different energy. Previous work suggested that the NIEL of a particle closely correlated with the damage it creates. Measuring the gain degradation as the function of the fluence and applying the Messenger-Spratt equation we can calculate a damage factor. We can compare the damage factors of heavy ions to the damage factors of neutrons and this will give us the damage equivalency. We compared the results for several ion-energy combinations to similar measurements carried out with ultra short high neutron flux pulses at the Los Alamos Neutron Science Center (LANSCE). The details of these experiments including the description of the LANSCE experiments are in ref. [8]. Here we will just summarize the results.

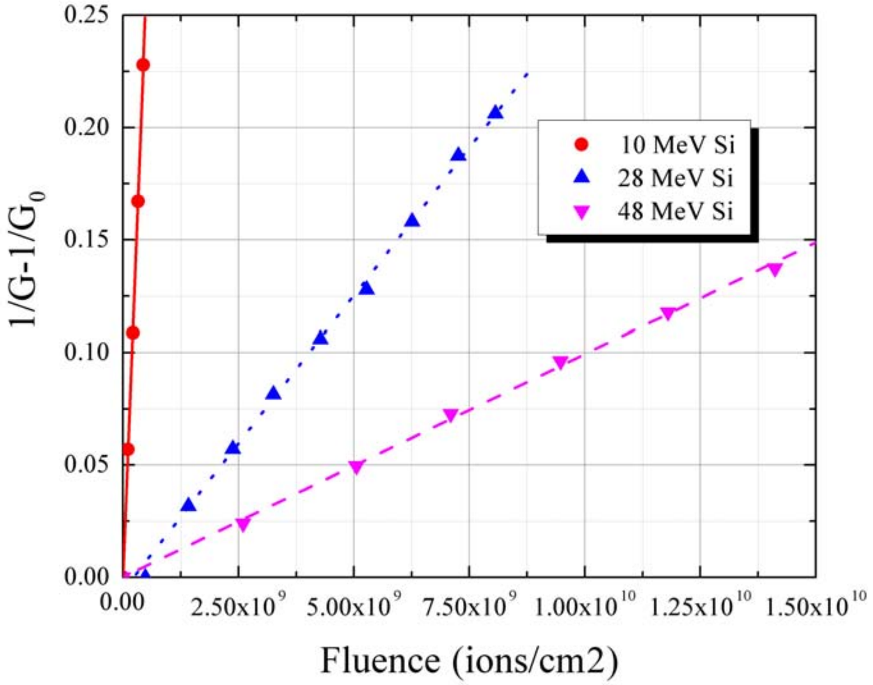

Figure 15 Inverse gain degradation as the function of fluence for Si beams with different energies. All the points are on straight lines as predicted by the Messenger-Spratt equation.

Figure 15 shows the inverse gain degradation dependence on the fluence for three different Si beams. At these gain degradation levels the measured inverse gain degradations line up with straight lines with different slopes as the Messenger-Spratt equation predicted. The 10 MeV Si has the largest slope (largest damage factor), the peak of the damage profile is at the emitter-base junction. The damage in the emitter-base junction effects the gain by increasing recombination; therefore, increasing the base current.

Figure 16 shows the same data re-plotted as the function of the 1 MeV neutron fluence. The 1 MeV equivalent neutron fluence (Φ_n) was calculated using equation (1.4), where k_{ion} is the damage factor from Figure 15, k_n is the damage factor from the LANSCE measurements (shown in Figure 16), and Φ_{ion} is the measured ion fluence.

$$\Phi_n = \frac{k_{ion}}{k_n} \Phi_{ion} \qquad (0.4)$$

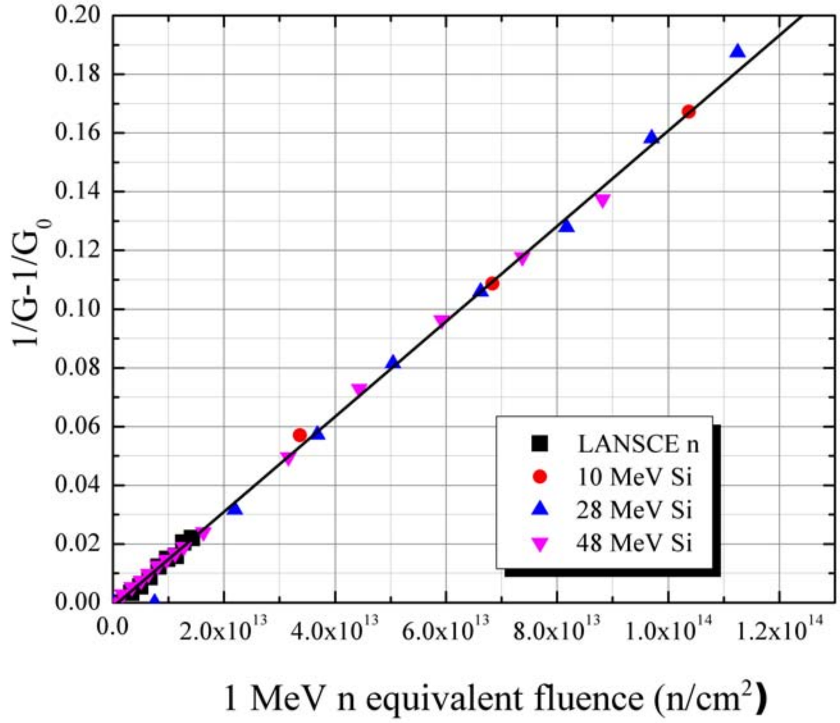

Figure 16 Inverse gain degradation as the function of 1 MeV neutron equivalent fluence. The neutron data from LANSCE is shown with black squares. The 1 MeV neutron equivalent fluence was calculated using equation (0.4).

Table 1 Damage factors, NIEL, and their ratios to neutron damage factors (LANSCE) and NIEL from ref 6.

Current	Particle	k	k/k_n	NIEL	$NIEL/NIEL_n$
0.22 mA	LANSCE	1.6×10^{-15}	1	95[6]	1
0.22 mA	He (12 MeV)	1.0×10^{-13}	70	8000	84
0.22 mA	Si (10 MeV)	5.2×10^{-10}	330,000	4.6×10^{7}	480,000
0.22 mA	Si (28 MeV)	2.8×10^{-11}	18,000	2.1×10^{6}	22,000
0.22 mA	Si (48 MeV)	1.3×10^{-11}	8,100	9.9×10^{5}	10,000

Table 1 shows the damage factors for various ion beams and for the LANSCE neutrons. The table also shows the calculated NIEL and its ratio to the 1 MeV neutron NIEL. We used the SRIM[5] binary collision program to calculate vacancy creation rates for ions. Then we converted the vacancy creation rates to NIEL using equation (1.5)

$$NIEL = \frac{2 \cdot dpa \cdot T_d}{0.8} \tag{0.5}$$

where dpa is the displacements per atom, and T_d is the displacement energy, 21 eV for silicon. The calculated NIEL ratios are in good agreement with the measured damage factor ratios. The largest deviation occurs for the 10 MeV Si. The reason for this is that this particular transistor has a 3D structure. Part of the emitter is covered with an Al electrode (~ 2 μm thick) another part is covered only with a thin field oxide (~ 0.4 μm). The 10 MeV Si ions have their damage peak in the emitter-base junction when they go through the Al electrode. This damage peak is much farther in the base when they go through the field oxide. Therefore, the damage levels at different parts of the emitter-base junction (below the Al electrode and below the field oxide) are very different; they differ about a factor of 10. If we use this correction then the k/k_n and NIEL/NIEL$_n$ values agree much better for the 10 MeV Si beam, too.

DEVIATIONS FROM THE MESSENGER-SPRATT EQUATION

Although, Figure 16 shows excellent agreement with the Messenger-Spratt equation we found serious deviations in two cases.

Light ions (ionization)

For light ions (hydrogen and helium) we found that the inverse gain degradation did not follow a linear behavior for low fluences. The main difference between the light and the heavy ions is the ionization to displacement ratio. The ionization has two effects in this particular device (2n2222 BJT). It creates electron hole pairs throughout the device. In the silicon these e-h pairs are swept out quickly producing photocurrent in the base and collector electrode. We did not find any effect of this photocurrent on the gain degradation. To separate the base and emitter electrodes a field oxide was put between the electrodes. When e-h pairs are created in the oxide the electrons are swept out quickly but the holes will be trapped. This creates a net positive charge in the oxide, which can lead to gain degradation. Similar effects were observed with X-ray and γ-ray irradiation where there is no displacement damage. Therefore, in case of ion irradiation the gain degradation is due to both trapped charge in the oxide and displacement damage in the base-emitter junction.

To separate the contribution of the ionization from the displacement damage we irradiated transistors in the Gamma Irradiation Facility (GIF) at SNL and measured the gain degradation as the function of dose. Figure 17 shows the inverse gain degradation as the function of dose. The effects starts to saturate around 1.5 MRad and the gain is not changing above 2 MRad. The reason for the saturation is that the oxide layer cannot trap more charge. Based on the above behavior we can empirically describe the gain degradation in a mixed environment with equation (1.6)

$$D = k \cdot \Phi + \alpha \cdot \left(1 - e^{-\frac{\Phi}{\Phi_0}} \right) \tag{0.6}$$

where k is the same as before (the damage factor due to displacement damage), α and Φ_0 are empirical parameters that have to be determined for each ion energy combination, device, and the operating parameters of the device. For heavy ions the first term is much larger than the second term, so this effect is negligible, cannot be observed. For light ions the two terms are comparable; therefore, the Messenger-Spratt curve is not linear initially.

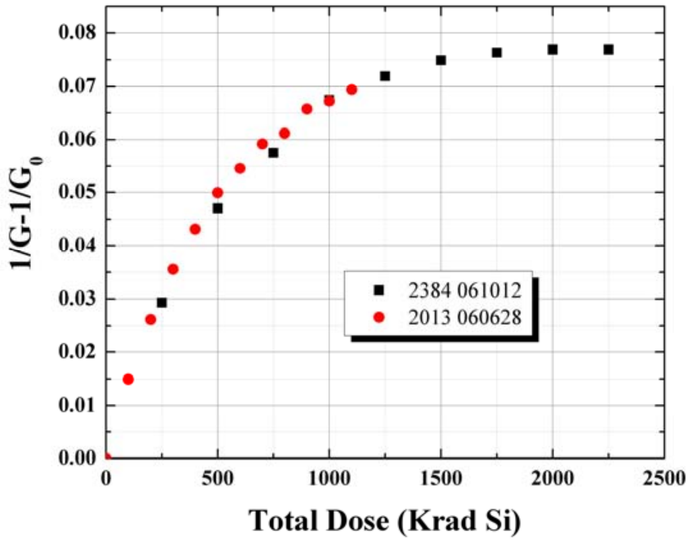

Figure 17 Inverse gain degradation as the function of gamma dose measured at the GIF facilty. The gain degradation saturates around 2 MRad.

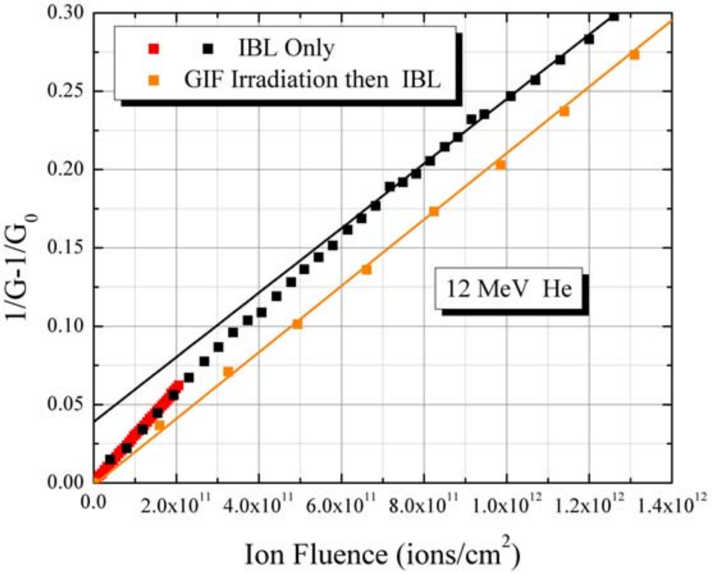

Figure 18 Inverse gain degradation versus fluence for 12 MeV He ions on virgin and pre-irradiated transistors. Notice that the curve of the virgin transistor becomes parallel with the curve of the pre-irradiated transistor abobe 8x10^{11} He/cm^2 fluence.

Figure 18 shows the Messenger-Spratt curves for 12 MeV He irradiation for two transistors. One was a virgin part and the other was pre-irradiated up to 2.5 MRad at the GIF facility. The figure shows that the gain degradation of the pre-irradiated transistor linearly depends on the fluence (the ionization effect already saturated). The virgin part starts out steeper than the pre-irradiated part and above ~8x10^{11} ions/cm^2 fluence the two curves become parallel. This clearly demonstrates that the gain degradation is due to the combined effect of ionization and displacement damage. A fit of equation (0.6) to the data of the virgin transistor results

$$k=\left(1.91\pm0.09\right)\cdot10^{-13}\quad \alpha=\left(6.5\pm1.6\right)\cdot10^{-2}\quad \Phi_0=\left(5.52\pm1.12\right)\cdot10^{11}\,.$$

Heavy ions (end of range effect in the collector)

In case of heavy ions at large fluences we also found deviation from the Messenger-Spratt equation. Figure 19 shows the inverse gain degradation as the function of the 1 MeV neutron equivalent fluence. Please note that the maximum of the fluence scale is ten times higher than in Figure 16. The 48 MeV Si curve follows the straight line (the 1 MeV neutron equivalent fluence was determined from Figure 16 for both the 28 and 48 MeV Si) but the 28 MeV Si curve deviates from the straight line and it is getting steeper with increasing fluence.

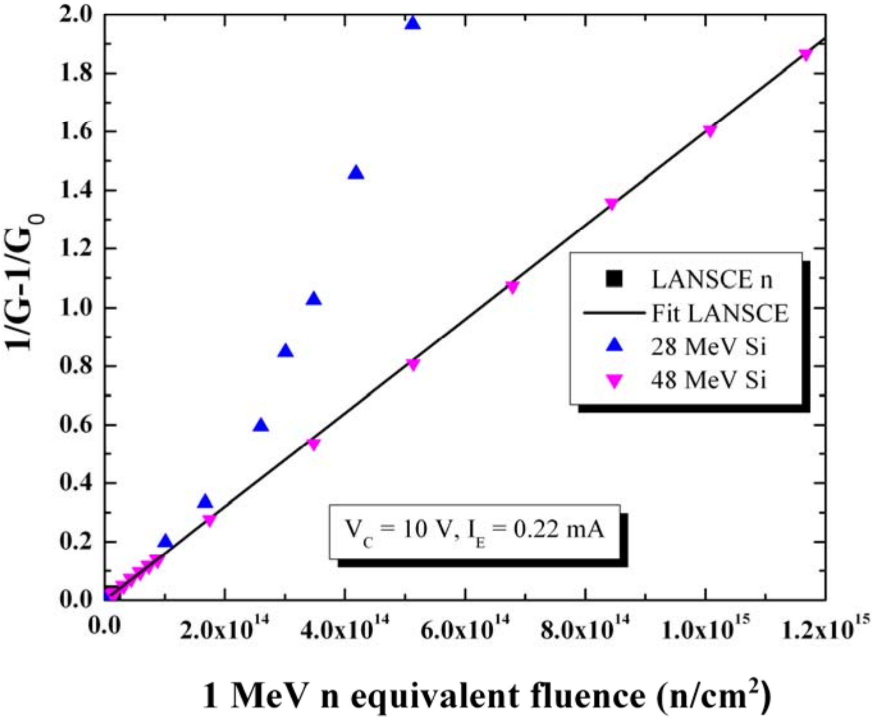

Figure 19 Inverse gain degradation for high fluences. The 28 MeV Si curve starts to deviate from the linear dependence around 1x10^{14} n/cm^2 equivalent fluence while the 48 MeV Si curve still follows the straight line at 1.2x10^{15} n/cm^2 equivalent fluence.

Capacitance measurements[9] showed that with the increasing fluence the doping level of the collector decreases. Figure 20 shows the damage profiles of the 28 and 48 MeV Si. The damage profile of the 28 MeV Si peaks in the collector, while the peak of the damage profiles of the 48 MeV Si is deep in the substrate. Taking the ratio of the of the two vacancy creation rates at the peak of the 28 MeV Si profile we see that the 28 MeV Si creates 35 times more damage than the 48 MeV Si. Since the collector is low doped at a certain fluence the damage becomes so large that the collector becomes compensated and the device stops functioning as a transistor.

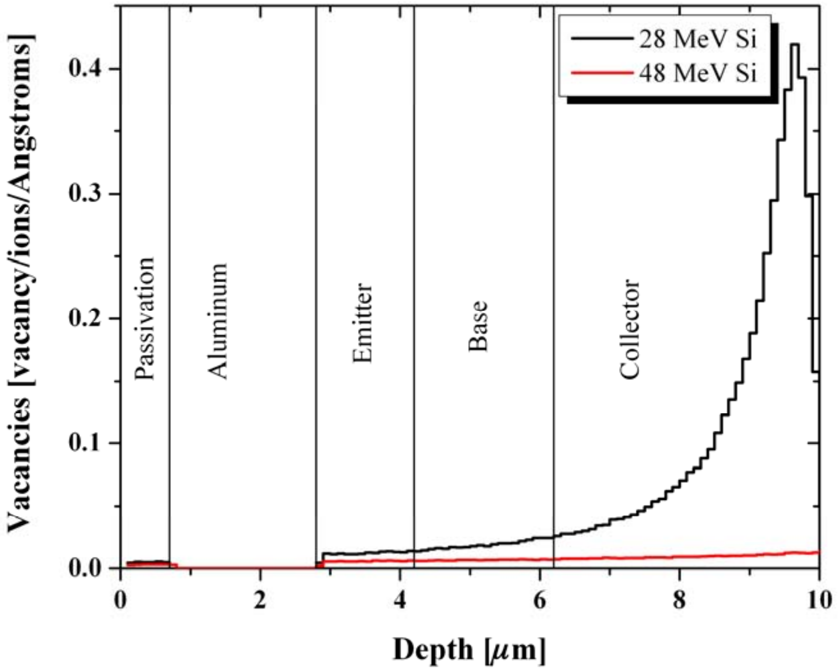

Figure 20 Damage profile of 28 MeV and 48 Mev Si in a 2n2222 BJT. Notice the large difference between the twoo profile in the collector.

DEEP LEVEL TRANSIENT SPECTROSCOPY (DLTS) RESULTS

DLTS is a technique that measures the number of defects and in conjunction with previous work in the literature, for example EPR, is used to identify the type of defect complex based on the characteristic temperature at which the DLTS peaks appear. A DLTS spectrum consists of measurements of the characteristic changes in the capacitance of a p-n junction as a function of temperature. The capacitance changes result from the filling and emptying of the defect complexes.

We have performed and compared DLTS measurements neutron, heavy and light ions, as well as gamma irradiated devices. While the DLTS spectrum is very similar for neutron and heavy ion irradiation, an anomalous peak is observed for proton, He and gamma irradiation. This anomalous peak has been associated with ionization damage in this series of devices.

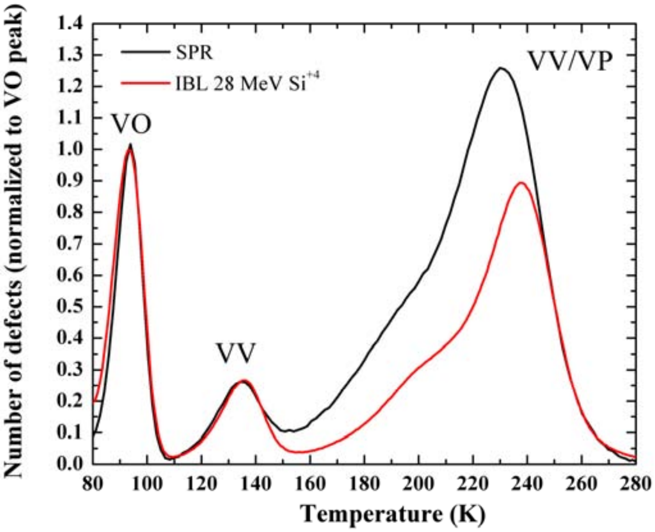

Figure 21 DLTS spectrum for two samples, one irradiated with a fast neutron fluence of ~ 1 x 1014 n/cm2, the second irradiated with heavy ions (28 MeV Si+4) to a final gain of ~20. Both spectra show three main peaks at the following temperatures: 95 K (VO), 140K (VV) and 240K (VP) for a correlator setting of 0.1 ms. We have normalized the spectrum to the VO peak in both cases to aid in comparison. Strikingly, the VO and VV are in excellent agreement while the difference between the VV/VP peak is currently under investigation.

In Figure 21 we show a comparison between a DLTS spectrum taken after irradiation with fast neutron from the Sandia Pulsed Reactor (SPR-III) and a heavy ion irradiation. We observe the common silicon complex defects including the vacancy-oxygen (VO), the silicon di-vacancy (VV) and the vacancy-acceptor, here vacancy-phosphorus (VP). We have normalized each spectrum to the VO peak to aid in comparison. As can be seen in the spectrum the high temperature peak consists of at least two different defect complexes (the deep VV and the VP with other possibilities as well).

Figure 22 shows DLTS spectrum for both heavy and light ion irradiations. Whereas, the heavy ion irradiation has similar structure to neutron irradiation the light ion irradiation shows an additional peak at 170 K. This additional peak does not correspond to an additional defect complex, but rather is associated with ionization damage to the oxide layer in this series of devices.

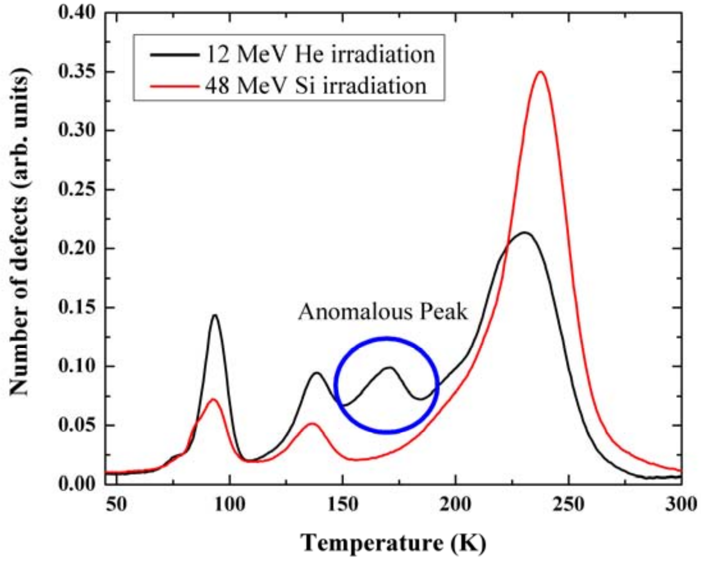

Figure 22 DLTS spectrum for two samples, one irradiated with 48 MeV Si to a ion fluence of $3.0x10^{10}$ ions/cm^2, the second irradiated with a 12 MeV He to an ion fluence of $9.4x10^{12}$ ions/cm^2. Both spectra show three main peaks at the following temperatures: 95 K (VO), 140K (VV) and 240K (VP) for a correlator setting of 0.1 ms. The additional peak between the VV and VP peak in the helium irradiation is associated with ionization. This additional peak shows no dependence on the DLTS correlator setting.

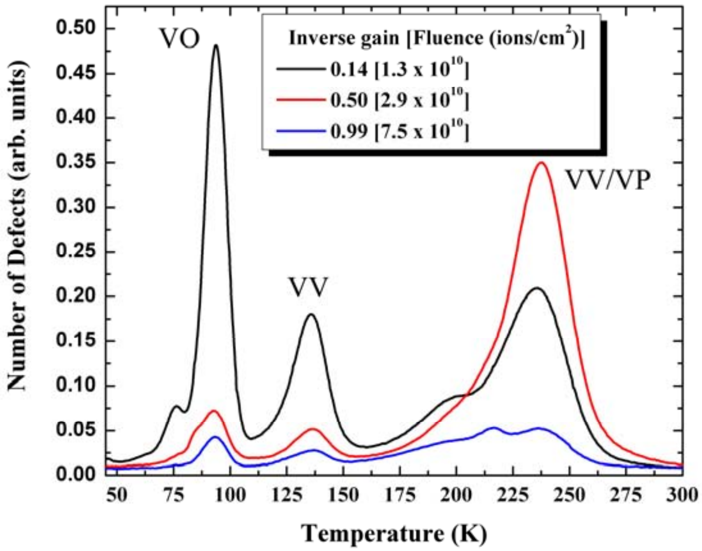

Figure 23 DLTS spectra 48 MeV Si^{+7} irradiation for three different fluences. For inverse gain degradation less than 0.50 we observe a linear increase in the VP with fluence. For higher fluence values the DLTS amplitude changes dramatically.

Figure 23 shows a series of DLTS spectra for a 48 MeV Si^{+7} irradiation. We observe the common silicon complex defects including the vacancy-oxygen (VO), the silicon di-vacancy (VV) and the vacancy-acceptor, here vacancy-phosphorus (VP). We observe an increase in the VP complex which scales linearly at low fluence. We believe that the decrease in the observed amplitudes of the VO and shallow VV peaks is due to defect clusters at higher fluences. Coulomb repulsion from nearby occupied VO and VV traps prevents the filling of these shallow levels in highly damaged material. For the highest fluence we observe a dramatic decrease in the amplitude of all the DLTS peaks. This decrease is believed to be caused by overlapping defect clusters in the collector causing the average doping, derived from capacitance-voltage curves, to drop.

While the general structure of the DLTS plots (Figure 21) are the same for the different irradiation types one of the keys differences is the number of VP per initial defect formed in the neutron irradiation is much larger than the VP per initial defect formed in the heavy ion irradiation. While we do not yet have a definitive explanation of this effect we will consider two possible causes: ionization and micro-structure. Consider first that the irradiation with the largest VP per initial defect the neutron sample has the lowest ionization, where as the heavy ion irradiation (larger ionization) shows the least VP per initial defect. This suggests the possibility that the less ionization during the irradiation larger the number of VP formed due to the more-negative charge state of vacancy and an increased Coulomb attraction to phosphor. The ionization associated with the ion irradiation although large decreases dramatically at the end-of-range of the ion track. I.e., the 28 MeV Si which has it end-of-range in the collector of the device would have an effectively smaller ionization as compared to the 48 MeV Si which has its end-of-range in the device substrate. However, on-going experiments to change the effect of ionization during the neutron irradiation by exposing devices in forward and reserved-biased condition have failed to alter the observed VP spectrum. This implies that something else is driving the large VP effect in neutron other than ionization directly. A second explanation involves the microstructure of the clusters due to the irradiation. For ions near the end-of-range and neutrons are expected to be similar with large amounts of clustering. This implies that 28 MeV Si with its end-of-range in the collector should be more neutron like and the 48 MeV Si with its end-of-range in the substrate should be more electron like, and indeed this is observed in the DLTS plots. However, one would expect that given the large concentration of vacancies and interstitials formed in close proximity to each other in the clusters that the chance of VP forming prior to the vacancy and interstitials winking out would be relatively small. Furthermore given that the dopant concentration of phosphor is 100 times less than that of oxygen we would expect lower amounts of VP per initial defect in the case of clusters. This is an interesting issue that must be figured out in order to more forward with the defect level modeling that is required for this project.

While the results shown in Figure 21 are very positive, indicating an ion-to-neutron equivalence in the DLTS, the dramatic changes in the resulting DLTS spectrum for the highest fluence 48 MeV Si^{+7} irradiation, as shown in Figure 3, are a cause for concern. Of issue is the depth profile of the damage throughout the device. Neutrons have a very small collision cross-section with Si atoms (no Coulomb interaction), i.e., most neutrons pass through the device without striking a Si atom. Those that do strike a Si atom cause localized collision cascades. This results in uniform vacancy cluster creation throughout the depth of the device. On the other hand, ions lose energy as they travel deeper in the device because of both a large collision cross-section (nuclear-stopping power), and ionization (electronic-stopping power). The net result is that vacancy creation varies as a function of penetration depth. In this case, 48 MeV Si was chosen to ensure a relatively flat damage profile in the critical region of the device, namely the base-emitter junction. While 48 MeV Si has an end of range in the sample substrate there is a factor of two difference between the displacement damage (number of vacancies/ion/Å as calculated using SRIM-2003) at the base-emitter junction compared to the end of the collector. This is of importance because we are measuring the DLTS spectrum in the base-collector junction. From this discussion we draw the conclusion that DLTS amplitude does not scale at high fluence because the collector becomes compensated. The question then is: what is the appropriate metric for comparison between the ion and neutron irradiations?

SIMULATION RESULTS

Several types of simulations were performed using REOS.

Two sets of simulations focused on the effects of ionizing radiation on the oxide layer of a device[10]. In one set, the buildup of trapped charge is computed as a function of the total dose for a fixed dose rate. These results are shown in Figure 24. As the total dose increases, the total charge increases linearly at first. However, at a high total dose the charge saturates because the additional electrons and holes recombine with the existing charge.

Figure 25 shows the dose rate dependence of the buildup of interface traps. At low dose rates, the injected electrons and holes are efficient at releasing hydrogen from source sites. However, at high dose rates the increased electron-hole plasma density causes electrons to recombine with the holes before the hydrogen is released. Thus fewer interface traps are created.

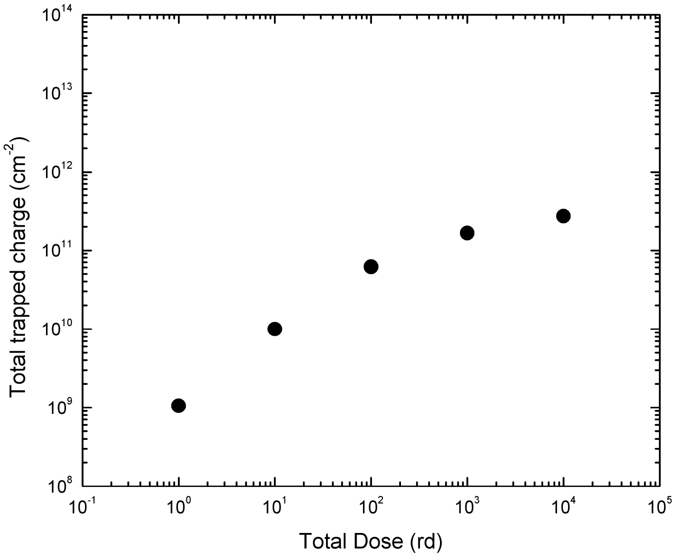

Figure 24: The total charge as a function of total dose for an oxide layer.

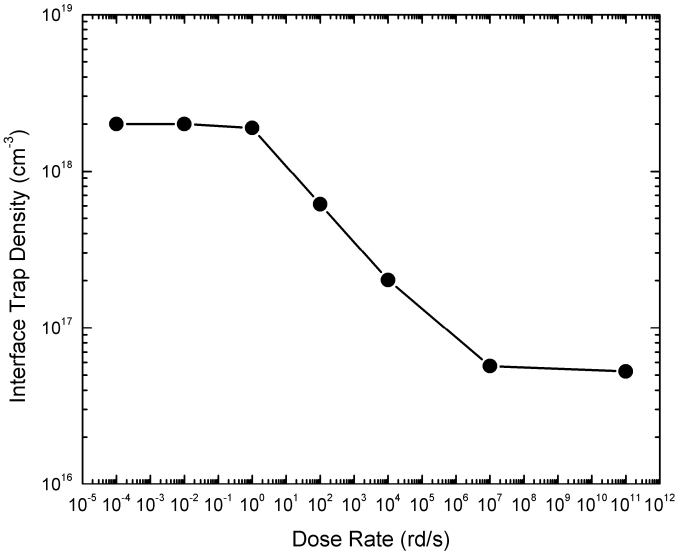

Figure 25: Interface trap density as a function of dose rate.

Several sets of simulations were performed to examine the effects of trapped charge on the carrier recombination in a device[11]. These simulations were performed on structures consisting of an oxide layer above a pn junction diode. Since the current flows along the interface, this structure captures the oxide physics in a bipolar transistor.

The results of these calculations are shown in Fig. 26. This figure shows the diode current with and without the trapped charge. For these particular calculations, the effects of the trapped charge were obtained by applying an external voltage to the gate of this diode. This structure is motivated by numerous studies of gated diodes and the literature describing the effects.

The primary effect of the trapped charge is at low forward bias on the diode. In this case, most of the current is in a region near the interface. As the forward bias increases, the contribution becomes smaller because other portions of the diode contribute to the current.

Several sets of simulations focused on the effects of transient annealing[11]. These simulations included the effects of recombination enhanced defect reactions on interstitial migration. These simulations were motivated by the need to explain injection level dependent annealing of transistor gain.

These simulations assume a short burst neutron pulse that generates interstitials, vacancies and divacancies. The parameters governing the annealing were obtained from the literature.

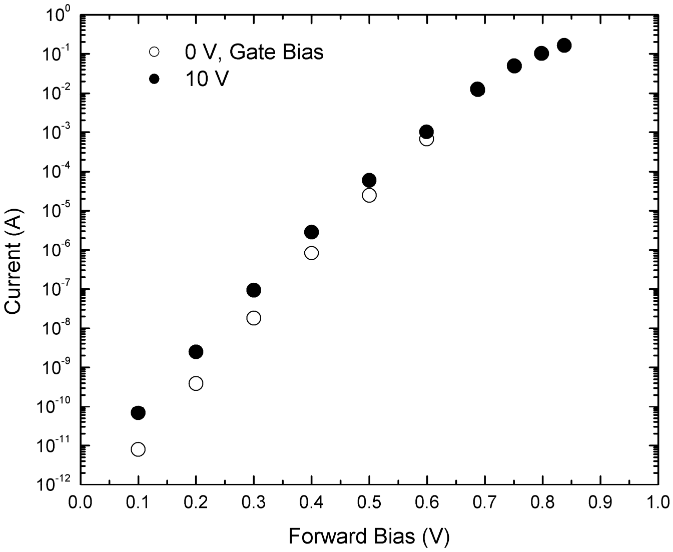

Figure 26: Shows the effect of trapped charge on carrier recombination at bulk traps

Figure 27 shows the recombination rate as a function of time for three different injection rates. It includes contributions from the three species, vacancies, interstititials and divacancies. The more rapid change of the rate as the injection rate increases follows from the more rapid annealing of the interstitials. This effect is in qualitative agreement with the effect of injection rate seen in the two sets of data. Furthermore, the injected carrier density is similar for the theory and the experiments but further work is needed for this assessment because the carrier density depends on how much annealing has occurred.

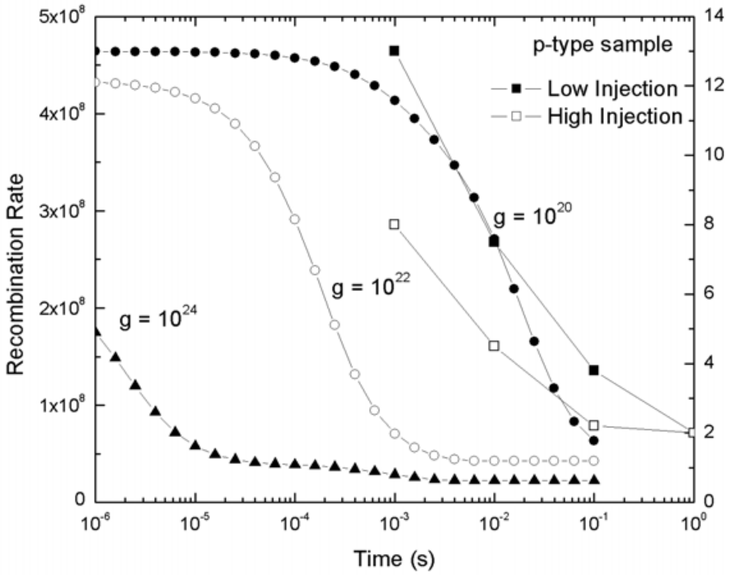

Figure 27 : Shows a comparison of the simulations with transient annealing data for solar cells taken at two different injection rates.

The main contribution to the recombination rate at short times is due to interstitial recombination. The evolution to shorter times with increasing carrier injection is due to the increased athermal diffusion stimulated by the carrier recombination at the interstitials. The time-scale of vacancy evolution is nearly independent of injection rate. At the highest injection level, substantial interstitial annealing occurs before vacancy annealing. Thus the vacancy contribution shows up as a plateau in that simulation.

Comparing the theory with the data reveals that the data have a more gradual evolution than that seen in the calculations. This may be due to contributions from competing processes not included in this minimal simulation.

Finally, another set of simulations focused on direct simulation of DLTS experiments. This set of simulations was motivated by the need to understand the DLTS signal from samples whose defects have a non-uniform distribution due to end-of-range effects.

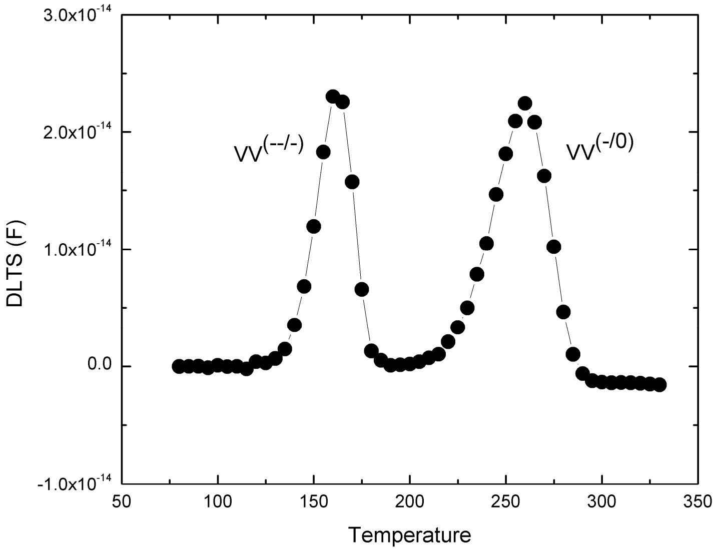

Figure 28 : Simulations of DLTS spectra for divacancy defects in a diode.

Figure 28 illustrates the results of these simulations. This figure shows the DLTS signal from a sample with divacancy defects.

SUMMARY

We have shown that heavy ions can be useful in the simulation of neutron displacement damage. A new methodology was worked out and damage equivalence was established between neutrons and ions. We discovered that the Messenger-Spratt curve for light ions does not follow the predicted linear behavior for low fluences. We showed that the non-linear behavior is due to trapped charge in the field oxide. We showed that the gain degradation can be decomposed into degradation due to trapped charge in the oxide and to displacement damage. The gain degradation due to the trapped charge exponentially saturates with fluence while the gain degradation due to displacement damage is linear with fluence. For heavy ions the displacement damage is much larger than ionization and this is why the Messenger-Spratt curve is linear. In case of light ions the two terms are comparable and this causes a superlinear behavior for low fluences. We also found that the gain degradation is not linear with fluence at higher fluences depending on the ion species and energy used. The reason for the non-linearity is the high level of damage in the collector which leads to the compensation of the collector, or even to the amorphization of silicon.

We have compared ion and fast neutron irradiations to determine an ion-to-neutron damage equivalence. We found that a combination of metrics is needed to ensure a comprehensive understanding of the physics involved in the ion-to-neutron conversion. These metrics are: the transistor gain and the number of defects from DLTS. While the inverse gain degradation is linear to the highest measured fluence this metric is primarily probing the base-emitter junction and is not indicating the collector compensation that occurs, as evident in the DLTS spectra.

The methodology developed in this work is used now in QAPSR (Qualification Alternatives for SPR) program routinely.

The ultimate conclusion of this LDRD is probably that more work will be required to establish the physics of damage equivilance between effects produced by MeV neutrons and MeV ions, e.g. Si. However, it is clear from the research performed on this LDRD that for the same NIEL or 1 MeV equivalent neutron fluence up to 4e14/cm2, as calculated by SRIM-2003, that the inverse gain degradation (Eq. 1.1) and the number of vacancies calculated from the VP peak agree within a factor of 2.

REFERENCES

---

[1] J. R. Srour, C. J. Marshall, and P. W. Marshall, “Review of displacement damage effects in silicon devices”, IEEE Trans. Nucl. Sci. vol. 50, pp 653-670, 2003.

[2] G. P. Summers, C. J. Dale, E. A. Burke, E. A. Wolicki, P. W. Marshall, and M. A. Gehlhausen, “Correlation of particle-induced displacement damage in silicon”, IEEE Trans. Nucl. Sci. vol. 34, pp 1134-1139, 1987.

[3] G. C. Messenger and J. P. Spratt, “The effects of neutron irradiation on silicon and germanium”, Proc. IRE vol. 46, pp 1038-1044, 1958.

[4] J. H. Warner, S. R. Messenger, R. J. Walters, and G. P. Summers, “Displacement damage correlation of proton and silicon irradiation in GaAs”, IEEE Trans Nucl. Sci. vol. 52, pp 2678-2682, 2005.

[5] www.srim.org

[6] ASTM Standard Methods E721-85 and ER2-85, Annual Book of ASTM Standards, ASTM, Philadelphia, Vol. 12.02, 1988.

[7] Standard Test Method for Use of 2N2222A Silicon Bipolar Transistors as Neutron Spectrum Sensors and Displacement Damage Monitors.”

[8] E. Bielejec, G. Vizkelethy, N.R. Kolb, D.B. King, and B.L. Doyle, “Damage Equivalence of Heavy Ions in Silicon Bipolar Junction Transistors”, IEEE Trans. Nucl. Sci., in print.

[9] Robert M. Fleming, Private communications

[10] H. P. Hjalmarson, R. L. Pease, C. E. Hembree, R. M. Van Ginhoven and P. A. Schultz, “Dose-rate dependence of radiation-induced interface trap density in silicon bipolar transistors, Nucl. Instrum. Methods Phys. Res., Sect. B, Vol. 250, 269 (2006).

[11] H. P. Hjalmarson, R. L. Please, R. M. Van Ginhoven, P. A. Schultz and N. A. Modine, Nucl. Instrum. Methods Phys. Res., Sect. B, accepted for publication.

Distribution:

1	MS 1322	H.J. Hjalmarson, 01435
1	MS 1056	B.L. Doyle, 01111
1	MS 1056	E.S. Bielejec, 01111
5	MS1056	G. Vizkelethy, 01111
1	MS1056	D.L. Buller, 01111
1	MS1415	R.M. Fleming, 01123
1	MS1146	D.B. King, 06771
1	MS1146	P.J. Griffin, 01384
1	MS1159	V. Harper-Slaboszewicz, 01344
1	MS1056	S.M. Myers, 01120
1	MS1056	W.R. Wampler, 01111
1	MS0427	R.A. Paulsen, Jr., 02118
1	MS1415	J.C. Barbour, 12930
2	MS 9018	Central Technical Files, 08944
2	MS 0899	Technical Library, 04536
1	MS0123	D.L. Chavez, LDRD Office, 01011